Submitted to the 29th International Conference on High–Energy Physics ICHEP98,
Vancouver, Canada, July 1998

Measurement of Leading Baryon Production at HERA and its Interpretation in terms of Colour Singlet Exchange

H1 Collaboration

Abstract

Deep–inelastic scattering events with a leading baryon have been detected by the H1 experiment at HERA using a forward proton spectrometer and a forward neutron calorimeter. Semi–inclusive cross sections have been measured in the kinematic region $2 \leq Q^2 \leq 50$ GeV^2, $6 \cdot 10^{-5} \leq x \leq 6 \cdot 10^{-3}$ and baryon $p_T \leq 200$ MeV, for events with a final–state proton with energy $580 \leq E' \leq 740$ GeV, or a neutron with energy $E' \geq 160$ GeV. The measurements are used to test production models and factorization hypotheses. A model of leading baryon production which consists of pion, pomeron and secondary reggeon exchanges gives a good description of both semi–inclusive cross sections in the region $E'/E_p \geq 0.7$, where E_p is the proton beam energy. The model is used to constrain the pion structure function.

Abstract: 569
Parallel sessions: 5,4
Plenary sessions: 7,6

1 Introduction

We report the measurement of the semi–inclusive cross sections for proton and neutron production in deep–inelastic scattering (DIS). The $ep \to eNX$ data, where N represents either a final–state proton or neutron, were obtained during 1995 and 1996 using the HERA accelerator at DESY where 27.5 GeV positrons collide with 820 GeV protons. The events containing leading baryons were detected using the H1 detector upgraded with a forward proton spectrometer (FPS) and a forward neutron calorimeter (FNC).

The two general purpose experiments at HERA, H1 and ZEUS, have observed a class of events which are characterized by the absence of final–state particles in the region of phase space between the outgoing proton debris and the current jet [1, 2]. These so called rapidity gap events contribute approximately 10% to the total DIS cross section and can be interpreted as being due to interactions of a virtual photon with a pomeron [3, 4, 5]. In addition to virtual photon–pomeron interactions, one also expects meson exchanges to contribute to the total DIS cross section and to the production of leading protons and neutrons with small p_T [6, 7, 8, 9]. Due to its small mass the most obvious candidate for such an exchange is the pion. If only pion exchange is responsible for leading baryon production, the ratio of neutron and proton production should be equal to two due to the difference in the π^+ and π^0 coupling constants.

In this paper we present measurements of the semi–inclusive cross sections for proton and neutron production in the same kinematic region of x, Q^2 and p_T, where x is the Bjorken scaling variable, Q^2 is the negative four–momentum squared of the virtual photon and p_T is the transverse momentum of the final–state baryon with respect to the beam direction. The measurements are compared to the results of a Regge model of leading baryon production and are used to test the pion exchange expectation for the ratio of neutron and proton production. We also compare our measurements to the predictions of the LEPTO 6.5 Monte Carlo program [10] which simulates baryon production without Regge dynamics by using an alternative formalism based upon soft colour interactions [11, 12] and the string fragmentation model [13]. Our cross section measurements are relevant for the determination of fracture functions which are a perturbative QCD approach for describing the semi–inclusive production of hadrons in the proton fragmentation region [14, 15, 16].

We use the kinematic variables x, Q^2 and y to describe the inclusive DIS scattering process. They are defined as:

$$x = \frac{-q^2}{2p \cdot q} \qquad Q^2 = -q^2 \qquad y = \frac{p \cdot q}{p \cdot k}, \tag{1}$$

where p, k and q are the 4–momenta of the incident proton, the incident positron and the exchanged vector boson (γ^*) coupling to the positron. At fixed center–of–mass energy s they are related by $Q^2 = sxy$.

The kinematic variables [1] used to describe a final–state baryon are:

$$t = (p - p')^2 \simeq -\frac{p_T^2}{z} - (1-z)\left(\frac{m_N^2}{z} - m_p^2\right) \qquad z = 1 - \frac{q \cdot (p - p')}{q \cdot p} \simeq E'/E_p, \tag{2}$$

[1] This definition of t is different from previous H1 definitions of t, for example see reference [5], which defines t in terms of the hadronic system Y at the proton vertex. For leading baryon production the definition of t in this paper is more appropriate even though is is only equal to the momentum transfer for events where the final–state baryon is exclusively produced at the proton vertex.

where p' is the 4–momentum of the final–state baryon, m_N is the mass of the final–state baryon and m_p is the proton mass. The approximations given above for t and z are good to $\mathcal{O}(m_N^4/E_p^2)$ and $\mathcal{O}(m_N^2/E_p^2)$ respectively.

The four–fold differential cross section for baryon production can be parameterized by a semi–inclusive structure function, $\mathrm{F}_2^{LB(4)}$, defined by:

$$\frac{\mathrm{d}^4\sigma(ep \to eNX)}{\mathrm{d}x\,\mathrm{d}Q^2\,\mathrm{d}z\,\mathrm{d}t} = \frac{4\pi\alpha^2}{x\,Q^4}\left(1 - y + \frac{y^2}{2[1 + R(x, Q^2, z, t)]}\right)\mathrm{F}_2^{LB(4)}(x, Q^2, z, t), \tag{3}$$

where α is the fine structure constant and R is the ratio between the absorption cross sections for longitudinally and transversely polarized virtual photons. In the kinematic range covered by this analysis, the structure function $\mathrm{F}_2^{LB(4)}$ is rather insensitive to the value R and we assume that $R = 0$. The variation from $R = 0$ to $R = \infty$ leads to a 9% change at most in the value of $\mathrm{F}_2^{LB(4)}$.

The four–fold differential cross section integrated over $0 \leq p_T \leq 200$ MeV defines the semi–inclusive structure function $\mathrm{F}_2^{LB(3)}$ which we measure:

$$\begin{aligned}\frac{\mathrm{d}^3\sigma(ep \to eNX)}{\mathrm{d}x\,\mathrm{d}Q^2\,\mathrm{d}z} &= \int_{t_0}^{t_{\min}} \frac{4\pi\alpha^2}{x\,Q^4}\left(1 - y + \frac{y^2}{2}\right)\mathrm{F}_2^{LB(4)}(x, Q^2, z, t)\,\mathrm{d}t \\ &= \frac{4\pi\alpha^2}{x\,Q^4}\left(1 - y + \frac{y^2}{2}\right)\mathrm{F}_2^{LB(3)}(x, Q^2, z),\end{aligned} \tag{4}$$

where the integration limits are:

$$t_{\min} = -(1 - z)\left(\frac{m_N^2}{z} - m_p^2\right) \qquad t_0 = -\frac{(200\,\mathrm{MeV})^2}{z} + t_{\min}. \tag{5}$$

The symbols $\mathrm{F}_2^{LP(3)}$ and $\mathrm{F}_2^{LN(3)}$ denote the semi–inclusive structure functions for final–state protons and neutrons respectively.

2 Detection of Forward Baryons

The H1 detector is described in detail in references [17] and [18]. Here only the forward proton spectrometer and the forward neutron calorimeter will be described. The coordinate system convention used by the H1 experiment defines the positive z–axis, or "forward" direction, as being that of the outgoing proton beam. The positive x–axis points towards the center of the HERA ring.

2.1 Description of the Forward Proton Spectrometer

The proton data were collected during 1995 with the H1 forward proton spectrometer. In order to measure momenta of protons with scattering angles $\theta \lesssim 0.5$ mrad with respect to the beam, the HERA machine magnets adjacent to the interaction region are employed as spectrometer elements. Protons which have lost more than 10% of their energy in DIS interactions appear after about 80 m at a distance of several millimeters from the nominal orbit so that they can be registered in detectors close to the circulating beam. The detector elements are mounted inside movable vacuum sections, so called Roman Pots, which are retracted during injection and are brought close to the beam after stable luminosity conditions are reached. The Roman Pots approach the beam from above.

During 1995 H1 operated two FPS stations located 81 and 90 m away from the interaction point. Each station is equipped with four planes of scintillating fibre hodoscopes with u and v orientation ($\pm 45^\circ$ offset with respect to the y–axis). The scintillating fibre hodoscopes are 6 cm wide and 2.5 cm in height and are sandwiched between planes of trigger scintillators as sketched in Figure 1. Each scintillating fibre hodoscope has 240 scintillating fibres arranged in five densely packed layers. Four of the 1 mm diameter scintillating fibres, belonging to a common layer but separated by 11 fibres from each other, are attached to one cell of a 64 pixel position sensitive photomultiplier (Hamamatsu H–4139). Ambiguities in the hit combinations are resolved by using the segmented scintillators in front of and behind the hodoscopes.

The FPS detectors measure space points with a resolution of $\sigma_{\rm x} = \sigma_{\rm y} = 120\,\mu{\rm m}$. The two measurements at 81 and 90 m are combined into a track at 85 m, since there are no magnets between the stations. In both stations, ten out of the twenty layers have to show signals, in coincidence with trigger tiles, in order to reconstruct a track. The efficiency for a minimum ionizing particle to produce a hit in a layer is typically 61$\%$ and the track reconstruction efficiency is approximately 50$\%$. With the help of the transfer matrices of the magnetic channel, which are known with high accuracy between the interaction point and 85 m, trajectories are traced back to the interaction point and momenta are determined. Due to the fact that the HERA magnets lead to independent dispersion in both the horizontal and vertical planes, momenta can be measured twice by making use of the horizontal and vertical deflections. The two measurements have to agree within errors for tracks starting at the interaction point and this provides an efficient method for rejecting background tracks.

2.2 Calibration of the Forward Proton Spectrometer

In order to reconstruct momenta, the coordinates and slopes of scattered proton trajectories are transformed into a reference system with the circulating beam as the primary axis. As the actual beam position is not known with the required accuracy of less than 0.5 mm, an iterative procedure is adopted to determine the actual beam line for each fill. The nominal beam position serves as a first approximation, which is then corrected by minimizing the difference between the momenta measured in the horizontal and vertical planes of the HERA machine. In addition, the optimization process makes use of the fact that certain combinations of momenta and angles at 85 m are forbidden for particles coming from the nominal interaction vertex. Minimizing at the same time the difference between the horizontal and vertical momentum measurements, and the number of particles with "forbidden" combinations of slopes and positions at 85 m, the position of the circulating proton beam can be determined.

A maximum likelihood fit assuming nominal HERA optics is done for each fill in which the beam position and slope of the proton beam at the average detector position of 85 m are free parameters. This procedure, which has been verified by Monte Carlo simulations of the FPS, leads to a momentum resolution of typically $\sigma(E_p') = 6$ GeV at 700 GeV and an angular resolution at the interaction point of $\sigma(\theta_{\rm x}) = 13$ μrad and $\sigma(\theta_{\rm y}) < 100$ μrad. The calibration of the FPS is described in more detail in reference [19].

The FPS calibration was checked using DIS events with a forward rapidity gap. For events with these characteristics the hadronic final–state is well contained within the central H1 detectors and one can compare the observed missing longitudinal momentum with the one measured by the FPS. The mean difference between the proton energy measured in the FPS and the energy expected from the calorimetric measurement is (-1.3 ± 8.9) GeV. From this we conclude that the scale of the FPS energy measurement is correct within 9 GeV.

2.3 Description of the Forward Neutron Calorimeter

During 1996 the H1 experiment used a forward neutron calorimeter constructed of lead and scintillating fibres [20]. The calorimeter was originally built by the LAA project [21] and used by the WA89 experiment at CERN [22, 23]. Before installing the calorimeter inside the HERA tunnel, it was necessary to reduce its weight and size. The modified calorimeter weighs approximately 10 metric tons and is located 107 m away from the nominal H1 interaction point. A schematic diagram of the FNC is shown in Figure 2.

The forward neutron calorimeter consists of interleaved layers of 2 m long lead strips and scintillating fibres. The lead to fibre volume ratio is 4:1 and the nuclear interaction–length λ_I is 21 cm. The scintillating fibres are 1 mm in diameter and are orientated approximately parallel to the direction of the incident neutron. The (1.7 ± 0.2) m attenuation length of the scintillating fibres has been measured using muons from cosmic events. Detailed GEANT [24] simulation studies have shown that this small attenuation length is responsible for the high–energy tail (see Figure 3) that we observe in the data.

The calorimeter is laterally segmented into hexagonal modules. Each module is defined by coupling 1141 scintillating fibres to a common photomultiplier located at the rear of the detector. The height of a hexagonal module is 8.6 cm. A gap between the top and bottom parts of the calorimeter is necessary in order to have space for the proton beam pipe which passes through the calorimeter. There are 67 modules in the bottom part of the calorimeter and 8 modules in the top part.

Two segmented planes of hodoscopes situated in front of the FNC are used to veto charged particles. Each plane is constructed of 1 cm thick hexagonal scintillator tiles which have the same lateral size as the calorimeter modules. The neutron detection efficiency of the FNC is $(93 \pm 5)\%$, the losses being due to accidental coincidences in the veto hodoscopes which mostly originate from the back–scattering of charged particles produced during the neutron's hadronic shower. This efficiency was determined by measuring the rate of signals in the hodoscopes as a function of the radial distance away from the neutron impact position.

All detector components, including the calorimeter and the hodoscope planes, are covered with lead sheets in order to shield them from synchrotron radiation.

2.4 Calibration of the Forward Neutron Calorimeter

The 75 modules of the FNC were initially calibrated at CERN using a 10 GeV incident electron beam. The FNC was positioned on a movable platform which allowed the response of each module to be measured separately. Preliminary calibration constants for the entire FNC were then determined by a matrix inversion procedure [25]. After this initial calibration, the FNC had an approximately uniform response independent of impact position.

After the calorimeter was installed in the H1 beam line, run–dependent calibration constants were determined every few weeks by comparing the energy spectrum of neutrons, observed in interactions between the proton beam and residual gas in the beam pipe, with the results of a $pp \rightarrow nX$ Monte Carlo simulation based upon pion exchange. Hadronic $pp \rightarrow nX$ data, obtained by the ISR and by other experiments at CERN [26, 27], are well described by pion exchange and have been used to constrain the pion flux factor [28, 7]: as the pion flux factor determines the energy spectrum of final–state neutrons by comparing with the Monte Carlo simulation we are effectively calibrating the FNC with respect to previous experimental results. In the $pp \rightarrow nX$ Monte Carlo program, the acceptance and the energy response of the FNC are simulated by tracking neutrons through the GEANT [24] simulation of the H1 beam line.

Figure 3a shows the uncorrected neutron energy spectrum observed in proton beam–gas interactions compared to the results of the Monte Carlo simulation. The two distributions are normalized to the same number of entries above 500 GeV. The peak position and the high–energy tail observed in the data are in good agreement with the simulation. Figure 3b shows the same beam–gas energy spectrum normalized to the neutron energy spectrum observed in DIS interactions. Above 300 GeV, where trigger threshold effects do not matter, the two distributions again agree very well in shape. This comparison, between proton beam–gas interactions, DIS interactions and a pion exchange Monte Carlo simulation is the method we use to calibrate the FNC. We estimate a 5% energy scale uncertainty for the FNC based upon our comparison between proton beam–gas interactions and the pion exchange Monte Carlo simulation.

The short–term gain variation of the FNC photomultipliers is measured by a LED monitoring system. The light from seven light–emitting–diodes is coupled by optical fibres to the entrance windows of all the photomultipliers. The average response of the FNC photomultipliers to the LED light is used on a run–by–run basis to correct for small changes in the gain of the FNC photomultipliers. When there are stable beam conditions, the gain variation of the FNC photomultipliers is typically less than 0.1% during 30 minutes.

The spatial resolution of the FNC was determined using three small scintillator counters situated in front of the calorimeter. The scintillators are $3 \times 3 \times 10$ mm^3 and they are used in coincidence with a hodoscope tile to define a trigger. The spatial resolution of the FNC was determined to be:

$$\sigma_{xy}(E) = \frac{5.13 \pm 0.81}{\sqrt{E\,[\mathrm{GeV}]}} + (0.22 \pm 0.07)\,\mathrm{cm}, \tag{6}$$

where the reconstructed impact position was determined using the center–of–gravity of the hadronic shower and an empirical formula which corrects for the hexagonal shape of the calorimeter modules [29, 25].

3 Event Selection and Data Analysis

The proton and neutron data used to measure the semi–inclusive structure functions were collected during different years. The proton data were obtained during 1995 using a trigger which required a charged track through both detector stations of the FPS and a localized cluster in the backward (SPACAL) electromagnetic calorimeter. For part of the data a track candidate in the central jet chamber was also required by the trigger. During 1996, a trigger which required an energy deposit in the SPACAL electromagnetic calorimeter in coincidence with vertex trigger conditions was used to obtain the DIS data containing a high–energy neutron.

During the offline analysis selection, criteria were applied to the data in order to reduce beam related backgrounds and events due to photoproduction. Events from reactions in which the incoming positron lost a significant amount of energy by radiation were also discarded. The DIS selection criteria used in the analysis are:

- A positron with energy $E'_e \geq 12$ GeV in the angular range $156^\circ \leq \theta_e \leq 177^\circ$ was required which ensures that the scattered positron is within the acceptance region of the SPACAL electromagnetic calorimeter.
- The DIS kinematic variables were required to be in the range $2 \leq Q^2 \leq 50$ GeV^2, $0.02 \leq y \leq 0.6$ and $6 \cdot 10^{-5} \leq x \leq 6 \cdot 10^{-3}$. The kinematic variables are reconstructed using the Σ method [30] which combines the scattered positron's energy and angle measurements with the quantity Σ, which is the sum, over all hadronic final–state particles, of the differences between energy and longitudinal momentum. The Σ method has good resolution and keeps radiative corrections small over the entire kinematic range.
- The quantity $\sum_i(E_i - p_{z,i})$, which is calculated using the energy E_i and the longitudinal momentum $p_{z,i}$ of all final–state particles including the scattered positron, was required to be ≥ 40 GeV for the neutron analysis and ≥ 41.6 GeV for the proton analysis. These cuts suppress radiative events and photoproduction background.
- The reconstructed vertex position was required to be within ± 30 cm of the nominal vertex position in z.
- The proton analysis required at least one track with $p_T \geq 450$ MeV to originate from the interaction vertex.

Cuts related to the final–state baryons are:

- For the proton data, one forward proton track with $580 \leq E'_p \leq 740$ GeV and $p_T \leq 200$ MeV was required to be detected by the FPS. Fiducial cuts on θ_x and θ_y, that depended on the proton energy, were applied to ensure that the track was observed in a region of the phase space where the acceptance was well understood and stable over the run period.
- For the neutron data, one neutral cluster with $E'_n \geq 100$ GeV and $p_T \leq 200$ MeV was required to be reconstructed in the FNC.

After these cuts the data samples were grouped into 12 (x, Q^2) bins in the range $6 \cdot 10^{-5} \leq x \leq 6 \cdot 10^{-3}$ and $2 \leq Q^2 \leq 50$ GeV^2. The proton data sample consists of 1661 events and the neutron data consists of 10366 events. The total luminosities of the proton and neutron data samples are (1.44 ± 0.03) pb^{-1} and (3.38 ± 0.07) pb^{-1} respectively.

The acceptances of the FPS and the FNC were determined by Monte Carlo programs in which protons or neutrons from DIS reactions were tracked through a simulation of the HERA beam line. The finite aperture of the beam line magnets limits the acceptance of both the FPS and the FNC.

The FPS acceptance as a function of z was calculated using the RAPGAP Monte Carlo program which simulates pion exchange [31]. This Monte Carlo simulation gives a good description of the shape of the uncorrected data as shown in Figure 4a for the observed proton energy spectrum. The FPS acceptance is approximately 80% for protons with $0.76 \leq z \leq 0.90$ and $p_T \leq 200$ MeV. The LEPTO and ARIADNE [32] Monte Carlo programs were used to check that the FPS acceptance is independent of the assumed production model and to estimate the systematic uncertainties.

The corrected neutron energy spectrum was determined separately in each (x, Q^2) bin by using a regularized unfolding procedure [33]. The procedure uses Monte Carlo data to define a "resolution function" which is then used to correct the observed FNC energy spectrum for acceptance and migration effects. The LEPTO and RAPGAP Monte Carlo models were used to demonstrate that the unfolded neutron energy spectrum does not depend upon the production model used to define the resolution function. For neutrons with $z \geq 0.4$ and $p_T \leq 200$ MeV the FNC acceptance is $\gtrsim 30\%$.

Figures 4b and 4c show the observed neutron z and p_T spectra compared to the reweighted Monte Carlo data which result from the regularized unfolding procedure. The data and Monte Carlo z distributions, shown in Figure 4b, are in agreement by construction since the unfolding procedure does a fit to the data by reweighting the Monte Carlo as a function of z. The p_T distributions, shown in Figure 4c, demonstrate that the reweighted Monte Carlo gives a good description of a variable not used in the fit.

The semi–inclusive structure functions $\mathrm{F}_2^{LP(3)}$ and $\mathrm{F}_2^{LN(3)}$ have been corrected to the Born level. Radiative corrections were calculated using the program HERACLES [34]. In all (x, Q^2) bins they are smaller than 6%. We have included a 2% systematic error on our radiative corrections due to hadronic corrections and higher order processes which are not simulated by the HERACLES code.

Three types of systematic errors have to be considered: normalization errors, errors which depend on the final–state baryons and errors which are different for each (x, Q^2) bin:

- Normalization Systematic Errors
  - For the proton analysis the normalization error is 5.6%. The main contribution to this error is the 5.0% uncertainty in the proton reconstruction efficiency.
  - The normalization error for the neutron analysis is 5.7%. The 5.4% uncertainty in the neutron detection efficiency is the largest component of this error.

  The systematic errors on the total integrated luminosities, which are approximately 2%, are included in the normalization uncertainties.

- Final–State Baryon Systematic Errors
  - For the proton analysis, these errors are between 4.8% and 19.4%. Errors on the migration corrections, that depend upon the calibration procedure, range between 4.5% and 18.9%. Additional errors due to the uncertainty in the acceptance of the the fiducial cuts were evaluated by comparing the results obtained using the RAPGAP, LEPTO and ARIADNE Monte Carlo models.
  - The FNC energy spectrum, after being corrected for acceptance and migration effects by using the regularized unfolding procedure, has large systematic errors. We have varied the FNC energy scale by $\pm 5\%$ and reweighted the Monte Carlo data as a function of p_T to estimate these systematic errors. We have also used the zero

degree direction observed in the data and the shape of the impact point distribution to determine the FNC acceptance and a systematic error is applied corresponding to the difference between the two acceptance correction methods. These uncertainties lead to systematic errors which range between 25.9% and 57.9% for the corrected neutron energy spectrum.

- Errors which depend on x and Q^2
  - The systematic errors which differ in each (x, Q^2) bin range between 7.7% and 12.7% for the proton analysis. The uncertainties in the trigger efficiency and in the positron acceptance are the main contributions to these systematic errors. The uncertainty in the positron acceptance as a function of x and Q^2 was determined by varying the energy scale of the SPACAL calorimeter by $\pm1.5\%$, by varying the electron scattering angle by ±1 mrad and by simulating a 4% uncertainty in the measurement of Σ.
  - For the neutron analysis, the systematic errors which depend upon x and Q^2 range between 3.1% and 7.2%. The main source of these systematic errors is the uncertainty in the positron acceptance as a function of x and Q^2 which was determined by varying the energy scale of the SPACAL calorimeter by between $\pm1\%$ and $\pm3\%$ depending upon the energy of the scattered positron, by varying the energy scale of the LAr calorimeter by $\pm4\%$, and by varying the reconstructed angle of the scattered positron by ±0.5 mrad.

These errors can be compared with the statistical ones. The statistical errors for the proton analysis lie between 9.6% and 30.4% for 90% of the data points. For the neutron analysis, the statistical errors range between 4.7% and 29.2% for 90% of the data points.

4 The Semi–Inclusive Structure Functions $F_2^{LP(3)}$ and $F_2^{LN(3)}$

Our measurement of the semi–inclusive structure functions $\mathrm{F}_2^{LP(3)}$ and $\mathrm{F}_2^{LN(3)}$, for protons and neutrons with $p_T \leq 200$ MeV, are shown in Figures 5 and 6. The inner error bars show the statistical errors and the full error bars show the statistical and systematic errors added in quadrature. The data are compared to the predictions of the LEPTO and RAPGAP Monte Carlo models [10, 31].

The LEPTO 6.5 Monte Carlo program simulates baryon production using soft colour interactions and the JETSET string fragmentation model [10, 13]. Soft colour interaction models have been proposed to explain large rapidity gap events and the production of final–state baryons [11, 12]. In these models, the colour structure of the partons interacting with the virtual photon is modified by non–perturbative soft gluon exchanges which can lead to the production of colour neutral partonic subsystems separated in rapidity. After the fragmentation process, a high–energy baryon may be produced separated by a large rapidity gap from the remainder of the hadronic final–state.

The LEPTO Monte Carlo model describes the general shape and magnitude of the neutron data over the entire z range. It fails however to describe the rate of leading proton production and the rise in $\mathrm{F}_2^{LP(3)}$ as a function of Q^2. The leading order parton distributions for the proton by Glück, Reya and Vogt (GRV) [35, 36], and the default value of 0.5 as the probability for soft colour interactions, were used to calculate the LEPTO Monte Carlo predictions.

The RAPGAP Monte Carlo program simulates baryon production using pion exchange. In the Monte Carlo program, the cross sections for leading proton and neutron production are proportional to the product of the pion flux factor and the pion structure function. The pion flux factor determines the kinematics of the final–state baryons and is identical for proton and neutron production except for a factor of two. For the RAPGAP Monte Carlo predictions shown in Figures 5 and 6 we have used the pion flux factor determined by Holtmann *et al.* [7]. The rate of leading baryon production depends upon the values of the pion parton distributions and we have used the leading order parameterization by GRV [35, 36].

The RAPGAP Monte Carlo gives a good description of the high–energy neutron data with $z \geq 0.7$ but it fails to reproduce the absolute rate of proton production. In the low–energy region where the final–state baryon has $\lesssim 70\%$ of the incident proton's energy, the RAPGAP Monte Carlo program is not valid since additional physical processes, not simulated by the program, are expected to be the dominant production mechanisms.

It is interesting to compare the magnitudes of $\mathrm{F}_2^{LP(3)}$ and $\mathrm{F}_2^{LN(3)}$. For $z \geq 0.7$, the semi–inclusive cross section for proton production is larger than the cross section for neutron production in any specific (x, Q^2) bin. This result rules out pion exchange as the main production mechanism for leading protons since pion exchange models predict that the ratio of neutron and proton production should be equal to two.

5 Factorization and Scaling Violations of $F_2^{LP(3)}$ and $F_2^{LN(3)}$

Assuming that leading baryons emerge from reactions where the virtual photon is absorbed by a colourless object inside the proton, the structure function $\mathrm{F}_2^{LB(3)}$ should factorize into a flux factor $f(z)$ which is only a function of z, and a structure function $\mathrm{F}_2^{LB(2)}$ which depends upon β and Q^2. The quantity $\beta = x/(1-z)$ may be interpreted as the fraction of the exchanged object's momentum carried by the quark or gluon interacting with the virtual photon.

Alternatively one may assume models [11], which are not based on the exchange of colourless objects so that β can no longer be interpreted as a momentum fraction. In such scenarios, one might expect factorization in the variables x, Q^2 and z if the deep–inelastic scattering process off the proton is independent of the proton fragmentation.

To test both factorization hypotheses, fits were made to the data assuming the following general forms for $\mathrm{F}_2^{LB(3)}$:

$$\mathrm{F}_2^{LB(3)}(\beta,\, Q^2,\, z) = f(z) \cdot \mathrm{F}_2^{LB(2)}(\beta,\, Q^2) \tag{7}$$

$$\mathrm{F}_2^{LB(3)}(x,\, Q^2,\, z) = f(z) \cdot \mathrm{F}_2^{LB(2)}(x,\, Q^2), \tag{8}$$

where the discrete–function $f(z)$ is parameterized by free–parameters and where $\mathrm{F}_2^{LB(2)}$ is a polynomial in x or β, with simple $\log Q^2$ dependence, parameterized by additional free–parameters.

The fit results yield similar χ^2/ndf for both factorization hypotheses. A possible explanation for this result is the observation that for $x < 0.1$ the proton structure function is of the form

$F_2 \sim x^{-\lambda(Q^2)}$ [37]. This functional form does not change its shape when x is replaced by β. It should be noted however that the β and x variables are highly correlated, and that the data have thus relatively limited sensitivity to a difference of factorization in these two variables.

In order to quantify the scaling violations observed in the data, $F_2^{LP(3)}$ and $F_2^{LN(3)}$ have been fitted separately for each fixed value of β to the form:

$$F_2^{LB(2)}(\beta, Q^2) = a(\beta) + b(\beta) \cdot \log Q^2, \tag{9}$$

with Q^2 in GeV^2. The values of $b(\beta)/F_2^{LB(2)}$, which are a measure of the scaling violations, are plotted in Figure 7. Only the fit results which arise from the proton data with $z = 0.732$ and the neutron data with $z = 0.7$ are shown and the measurements of $F_2^{LP(3)}$ and $F_2^{LN(3)}$ in the lowest x bins have not been used since there is only a single Q^2 value. The data are compared to the scaling violations $dF_2/d(\log Q^2)/F_2$ seen in the inclusive structure functions of the pion and the proton. The pion and proton structure functions have been calculated using the GRV leading order parametrizations [35, 36]. The scaling violations observed in the semi–inclusive structure functions $F_2^{LP(3)}$ and $F_2^{LN(3)}$ are similar in size and shape and are close to those seen in the inclusive structure functions of the pion and the proton.

6 Comparison to a Regge Model of Baryon Production

Figure 8 shows a comparison between the leading baryon structure functions with $z \geq 0.7$ and a Regge model of baryon production. In the model, the contribution of a specific exchange process is determined by the product of the particle flux and its structure function evaluated at (β, Q^2). For leading baryon production with $p_T \leq 200$ MeV we therefore have:

$$F_2^{LB(3)}(\beta, Q^2, z) = \sum_i \left(\int_{t_0}^{t_{\min}} f_{i/p}(z,t)\, dt \right) \cdot F_2^i(\beta, Q^2), \tag{10}$$

where i denotes the pion, the pomeron and secondary reggeons (for example ρ, ω, a_2 and f_2). The integration limits t_0 and $t_{\min}$ are given by equation 5.

In the Regge model, we assume that the neutral pion, the pomeron and the f_2 all contribute to leading proton production. We neglect the contributions due to the additional secondary reggeons because they have been estimated to be much smaller than the contribution due to f_2 exchange [38, 39]. A comparison of total cross section measurements has resulted in the estimate that the flux of reggeons which have isospin equal to one (ρ and a_2) is only $\approx 3\%$ of the flux of reggeons with isospin equal to zero (ω and f_2) [38]. Regge theory also predicts f_2 dominance, among secondary trajectories in the present case, in contrast to exchange degeneracy for elastic scattering processes [39].

For leading neutrons, we assume that they are produced by charged pion exchange only. In the limited p_T range of the data, leading neutron production due to ρ and a_2 exchanges has been estimated to be more than an order of magnitude smaller than the contribution due to pion exchange [8]. Pomeron exchange also does not give a significant contribution since neutron production due to diffractive dissociation is believed to be $\approx 6\%$ of the pion exchange contribution [8]. The data sample has been used to estimate a 2% diffractive dissociation contribution to leading neutron production by determining the fraction of events with a large rapidity gap extending into the LAr calorimeter. We have neglected additional backgrounds such as neutron production due to resonance decays.

The pion, pomeron and reggeon flux factors have been determined using hadron–hadron data. The pion flux factor $f_{\pi/p}$ which we have used for neutron production is the same as the one used in reference [8]:

$$f_{\pi/p}(z,t) = C\frac{3g^2_{\pi Np}}{16\pi^2}(1-z)^{1-2\alpha'_\pi t}\frac{|t|}{(m^2_\pi - t)^2}\exp\left(2R^2_\pi(t-m^2_\pi)\right), \tag{11}$$

where $g^2_{\pi Np}/(4\pi) = 13.6 \pm 0.3$ [40], $\alpha'_\pi = 1$ GeV^{-2}, $R^2_\pi = 0.3$ GeV^{-2} and the Clebsch–Gordon coefficient is $C = 2/3$. For proton production via π^0 exchange we use the same flux factor with $C = 1/3$. The pomeron and reggeon flux factors are parameterized as [9, 38]:

$$f_{\mathbb{P}/p}(z,t) = \frac{54.4\,GeV^{-2}}{8\pi^2}(1-z)^{1-2\alpha_{\mathbb{P}}(t)}\exp\left(2R^2_{\mathbb{P}}t\right) \tag{12}$$

$$f_{\mathbb{R}/p}(z,t) = \frac{390\,GeV^{-2}}{8\pi^2}(1-z)^{1-2\alpha_{\mathbb{R}}(t)}\exp\left(2R^2_{\mathbb{R}}t\right), \tag{13}$$

where $\alpha_{\mathbb{P}}(t) = (1.08 + 0.25\,GeV^{-2}\,t)$ and $\alpha_{\mathbb{R}}(t) = (0.5 + 0.9\,GeV^{-2}\,t)$. The slopes are $R^2_{\mathbb{P}} = 1.9\,GeV^{-2}$ and $R^2_{\mathbb{R}} = 2\,GeV^{-2}$ respectively. The modulus squared of the signature factors have been absorbed into the couplings and we have not included reggeon–pomeron interference terms in the model.

The evaluation of the pion flux factor is not without some theoretical uncertainty. It has been pointed out that absorptive corrections, generated by double reggeon pion–pomeron exchanges, might play an important role in hadronic reactions in contrast to DIS. Since the pion flux factor which we have used was determined using $pp \to nX$ data, it might underestimate the flux of pions in the proton for DIS reactions by up to $\approx 30\%$ [41].

The structure functions for the exchanged particles are basically unknown in the low β region and one has to rely on theoretical models. For the pion structure function F_2^π we took the leading order parameterization by Glück, Reya and Vogt [35, 36]. For the reggeon and pomeron structure functions we assume $\mathrm{F}_2^{\mathbb{R}} = F_2^\pi$ and $\mathrm{F}_2^{\mathbb{P}} = (0.026/0.12)F_2^{\mathbb{R}}$ following the arguments given in reference [9]. Measurements of the diffractive structure function $\mathrm{F}_2^{D(3)}$ [3, 4, 5] only probe the pomeron at high β $(\beta > 0.04)$ and it is not possible to use these data to fix the pomeron structure function $\mathrm{F}_2^{\mathbb{P}}$ at the low β values of the semi–inclusive data $(\beta < 3 \cdot 10^{-3})$.

The model gives a good description of the neutron and proton data with $z \geq 0.7$. The rate of leading neutron production can be described entirely by π^+ exchange whereas the proton production data with $0.73 < z < 0.88$ require contributions from both f_2 and π^0 exchange. The contribution due to f_2 exchange is approximately a factor of two greater than the contribution due to π^0 exchange.

We use the measurement of $\mathrm{F}_2^{LN(3)}$ at $z = 0.7$ and the integral of the pion flux factor to constrain the pion structure function. Within the framework of the Regge model, the quantity $\mathrm{F}_2^{LN(3)}/\Gamma_\pi$ can be interpreted as being equal to the structure function of the pion where:

$$\Gamma_\pi(z=0.7) = \int_{t_0}^{t_{\min}} f_{\pi/p}(z,t)\,\mathrm{d}t = 0.131. \tag{14}$$

Figure 9 shows $\mathrm{F}_2^{LN(3)}/\Gamma_\pi$ as a function of β for fixed values of Q^2. The data are compared to predictions of several parametrizations of the pion structure function [35, 36, 42, 43, 44]. The latter are only shown in the Q^2 regions in which they are valid. The data are in good agreement with the expectations of the GRV leading order parametrization of the pion structure function. Background contributions and possible absorptive corrections, which have not been taken into account, would only affect the absolute normalization of our result since all of the data are at $z = 0.7$.

7 Conclusions

The semi–inclusive cross sections $ep \to epX$ and $ep \to enX$ have been measured in the kinematic region $2 \leq Q^2 \leq 50$ GeV^2, $6 \cdot 10^{-5} \leq x \leq 6 \cdot 10^{-3}$ and $p_T \leq 200$ MeV. Comparison of the proton and neutron data in the same kinematic domain shows that the production cross section for leading protons is larger than it is for leading neutrons. This result demonstrates that leading proton production cannot be entirely due to pion exchange.

The LEPTO Monte Carlo program, which is based upon soft colour interactions and a string fragmentation model, describes the magnitude and the general shape of the neutron data with $z \geq 0.3$. It fails however to describe the rate of leading proton production and the rise in the semi–inclusive structure function $\mathrm{F}_2^{LP(3)}$ as a function of Q^2. The RAPGAP Monte Carlo program, which simulates pion exchange, gives a good description of the neutron data with $z \geq 0.7$ but cannot explain the absolute rate of leading proton production.

The proton and neutron data are equally well described by fits assuming factorization in x, Q^2 and z or β, Q^2 and z. The scaling violations observed in the measured semi–inclusive structure functions $\mathrm{F}_2^{LP(3)}$ and $\mathrm{F}_2^{LN(3)}$ are similar in size and shape and are close to those seen in the GRV parametrizations of the inclusive structure functions of the pion and the proton.

The neutron and proton data are well described by a Regge model of leading baryon production which considers the colour neutral exchanges of pions, pomerons and secondary reggeons. The semi–inclusive cross sections for leading neutrons with $z \geq 0.7$ can be described entirely by π^+ exchange whereas the semi–inclusive cross sections for protons with $0.73 < z < 0.88$ require π^0 and f_2 exchange contributions. The contribution due to f_2 exchange is approximately a factor of two greater than the contribution due to π^0 exchange. The data are consistent with the GRV leading order parton distributions for the pion.

8 Acknowledgments

We are grateful to the HERA machine group whose outstanding efforts have made and continue to make this experiment possible. We thank the engineers and technicians for their work in constructing and now maintaining the H1 detector, our funding agencies for financial support, the DESY technical staff for continual assistance, and the DESY directorate for the hospitality which they extend to the non–DESY members of the collaboration. The forward proton spectrometer was supported by the INTAS93–43 project.

References

[1] ZEUS Collaboration, M. Derrick et al., *Phys. Lett.* **B315** (1993) 481.

[2] H1 Collaboration, T. Ahmed et al., *Nucl. Phys.* **B429** (1994) 477.

[3] H1 Collaboration, T. Ahmed et al., *Phys. Lett.* **B348** (1995) 681.

[4] ZEUS Collaboration, M. Derrick et al., *Z. Phys.* **C68** (1995) 569.

[5] H1 Collaboration, C. Adloff et al., *Z. Phys.* **C76** (1997) 613.

[6] J.D. Sullivan, *Phys. Rev.* **D5** (1972) 1732.

[7] H. Holtmann et al., *Phys. Lett.* **B338** (1995) 393.

[8] B. Kopeliovich, B. Povh and I. Potashnikova, *Z. Phys.* **C73** (1996) 125.

[9] A. Szczurek, N. N. Nikolaev and J. Speth, "Leading Proton Spectrum from DIS at HERA", FZJ–IKP–TH–97–22 (1997), hep–ph/9712261.

[10] G. Ingelman, A. Edin and J. Rathsman, *Comp. Phys. Comm.* **101** (1997) 108.

[11] W. Buchmüller and A. Hebecker, *Phys. Lett.* **B355** (1995) 573.

[12] A. Edin, G. Ingelman and J. Rathsman, *Phys. Lett.* **B366** (1996) 371.

[13] T. Sjöstrand, *Comp. Phys. Commun.* **82** (1994) 74.

[14] L. Trentadue and G. Veneziano, *Phys. Lett.* **B323** (1994) 201.

[15] D. de Florian and R. Sassot, "QCD Analysis of Diffractive and Leading–Proton DIS Structure Functions in the Framework of Fracture Functions", CERN–TH/98–109, hep–ph/9804240.

[16] M. Grazzini, L. Trentadue and G. Veneziano, *Nucl. Phys.* **B519** (1998) 394.

[17] H1 Collaboration, I. Abt et al., *Nucl. Instr. Meth.* **A386** (1997) 310, *ibid.* 348.

[18] H1 SPACAL Group, R.–D. Appuhn et al., *Nucl. Instr. Meth.* **A386** (1997) 397.

[19] B. List, Ph.D. Thesis, University of Hamburg (1997).

[20] Preliminary results determined using the 1995 H1 neutron calorimeter, which was used as a test, are in the proceedings of the 28th International Conference on High Energy Physics, pa02–063, Warsaw, Poland, July 1996.

[21] D. Acosta et al., *Nucl. Instr. Meth.* **A294** (1990) 193.

[22] WA89 Collaboration, Proposal to the SPSC CERN/SPSC–87/43, 1987.

[23] M. Beck et al., *Nucl. Instr. Meth.* **A381** (1996) 330.

[24] Application Software Group,"GEANT Detector Description and Simulation Tool", CERN Program Library Long Writeup W5013, October 1994.

[25] T. Nunnemann, Diploma Thesis, Universität Heidelberg, 1996.

[26] W. Flauger and F. Mönnig, *Nucl. Phys.* **B109** (1976) 347.

[27] V. Blobel et al., *Nucl. Phys.* **B135** (1978) 379.

[28] H. Holtmann et al., *Nucl. Phys.* **A596** (1996) 631.

[29] C. Scheel, Ph.D. Thesis, University of Amsterdam (1994).

[30] U. Bassler and G. Bernardi, *Nucl. Instr. Meth.* **A361** (1995) 197.

[31] H. Jung, *Comp. Phys. Commun.* **86** (1995) 147.

[32] L. Lönnblad, *Comp. Phys. Comm.* **71** (1992) 15.

[33] V. Blobel,"Unfolding Methods in High–Energy Physics Experiments", DESY Report: 84–118 (1984).

[34] A. Kwiatkowski, H. Spiesberger and H.–J. Möhring, *Comp. Phys. Comm.* **69** (1992) 155.

[35] M. Glück, E. Reya and A. Vogt, *Z. Phys.* **C67** (1995) 433; *Z. Phys.* **C53** (1992) 651.

[36] H. Plothow–Besch, *Comp. Phys. Comm.* **75** (1993) 396.

[37] H1 Collaboration, S. Aid et al., *Nucl. Phys.* **B470** (1996) 3.

[38] K. Golec–Biernat et al., *Phys. Rev.* **D56** (1997) 3955.

[39] Yu. M. Kazarinov et al., *Sov. Phys. JETP* **43** (1976) 598.

[40] R. G. E. Timmermanns, Th. A. Rijken and J. J. de Swart, *Phys. Rev. Lett.* **67** (1991) 1074.

[41] N.N. Nikolaev, J. Speth and B.G. Zakharov, "Absorptive Corrections to the One Pion Exchange and Measurability of the Small–x Pion Structure Function at HERA", KFA–IKP–TH–97–17 (1997), hep–ph/9708290.

[42] J.F. Owens, *Phys. Rev.* **D30** (1984) 943.

[43] P. Aurenche et al., *Phys. Lett.* **B233** (1989) 517.

[44] P.J. Sutton et al., *Phys. Rev.* **D45** (1992) 2349.

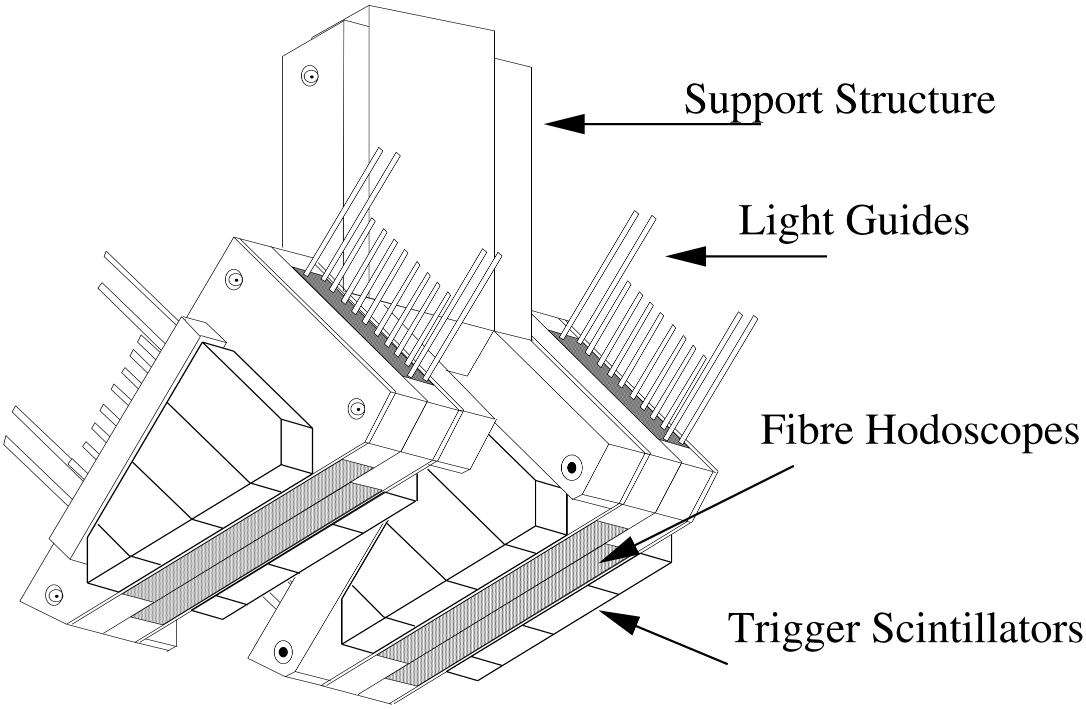

Figure 1: Perspective view of the scintillating fibre hodoscopes and the trigger scintillators inside a Roman Pot.

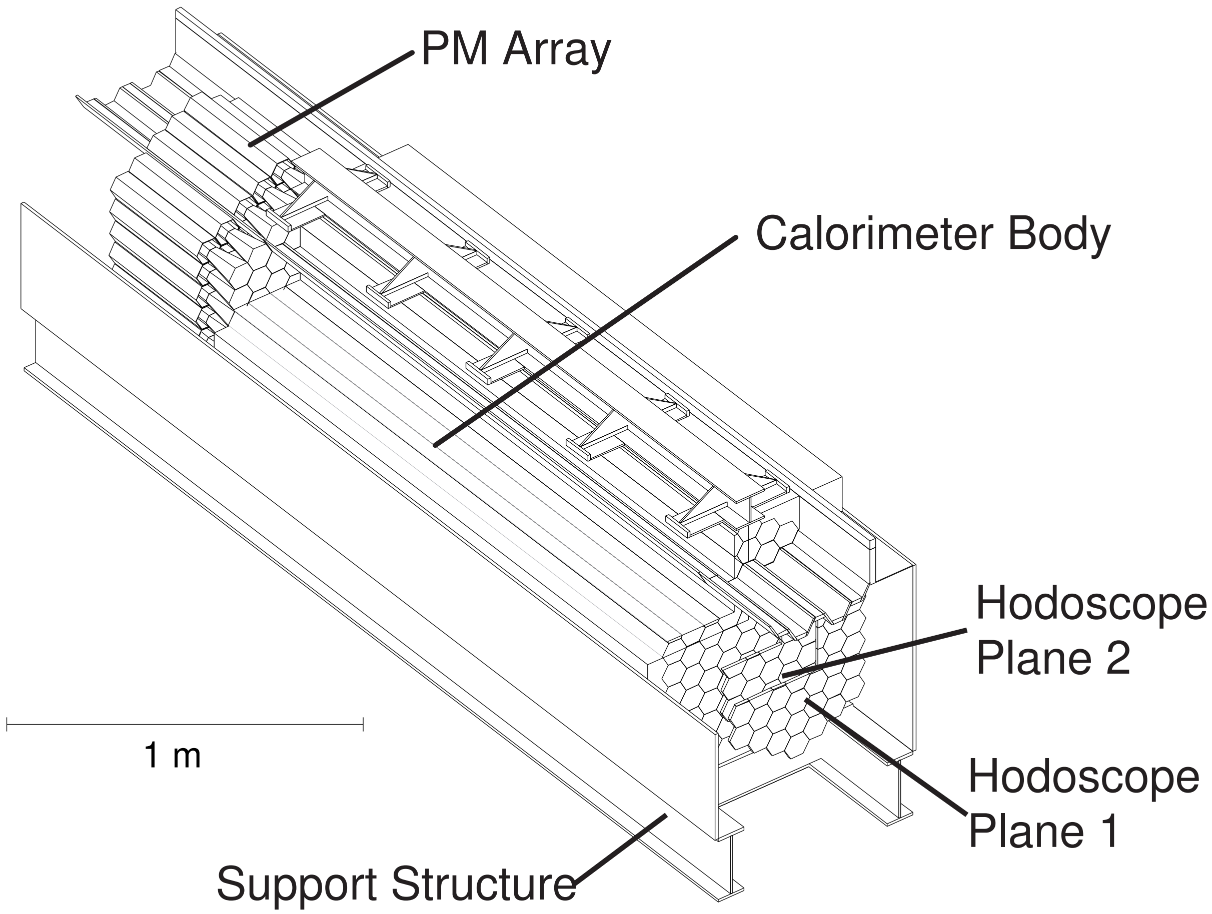

Figure 2: Configuration of the H1 forward neutron calorimeter.

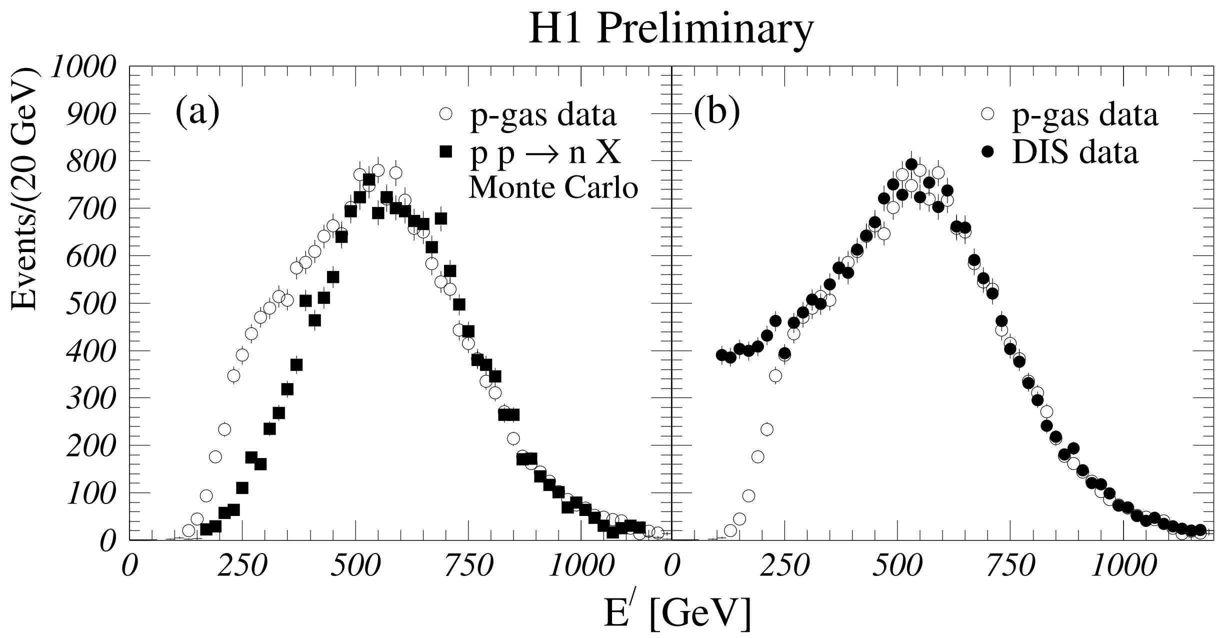

Figure 3: (a) The observed neutron energy spectrum in proton beam–gas interactions compared to the results of a $pp \rightarrow nX$ Monte Carlo simulation based upon pion exchange. The Monte Carlo simulation takes into account the acceptance and response of the FNC. (b) The same proton beam–gas energy spectrum compared to the neutron energy distribution observed in DIS interactions. The proton beam–gas energy spectrum has not been corrected for the trigger efficiency which is less than 100% below 300 GeV. All distributions are normalized to the same number of events with $E' \geq 500$ GeV.

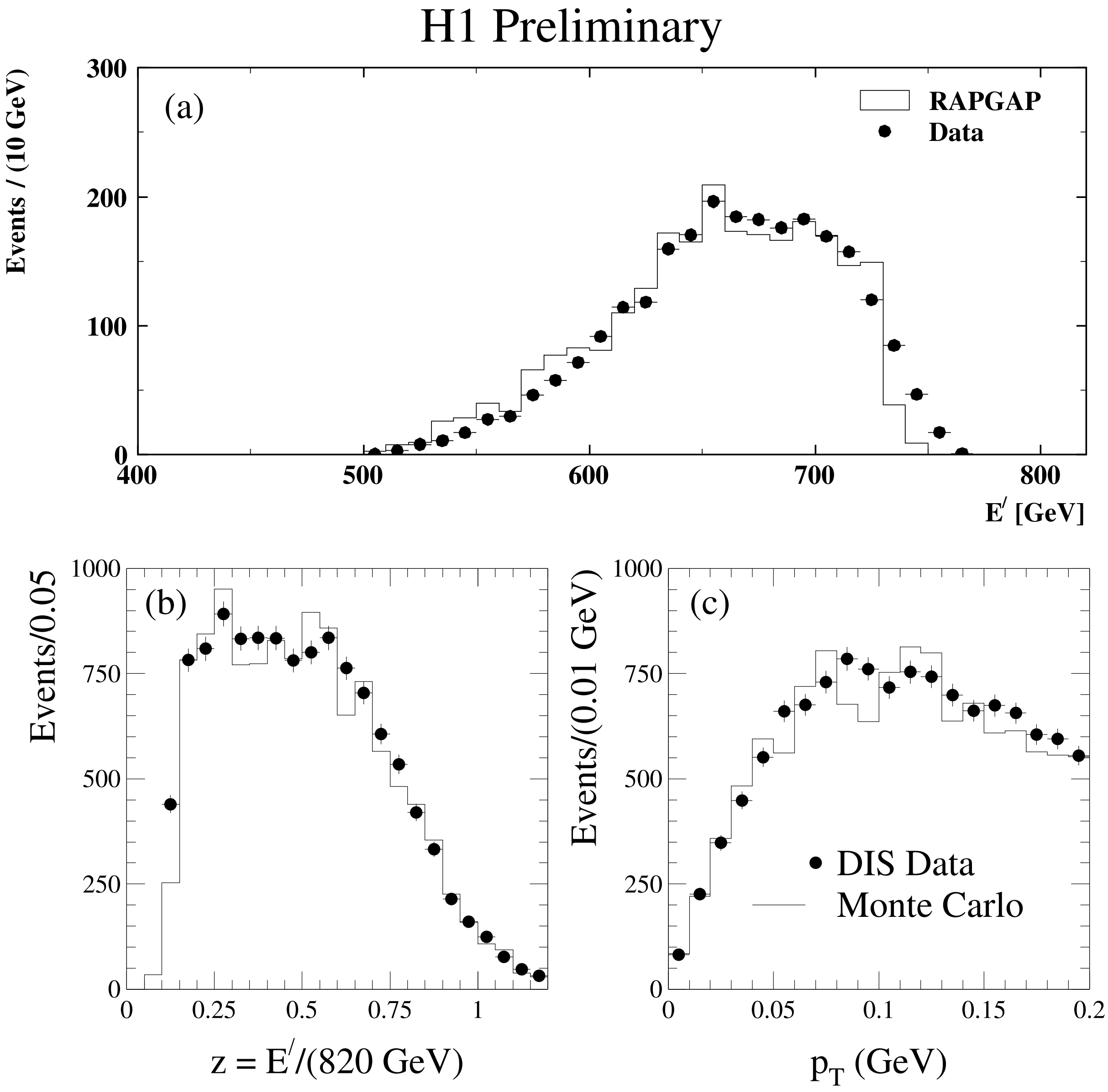

Figure 4: (a) The observed proton energy spectrum compared to reconstructed RAPGAP Monte Carlo data. In (b) and (c) the observed neutron z and p_T spectra are compared to reweighted Monte Carlo data which result from the regularized unfolding procedure. The Monte Carlo distributions are normalized to the total number of events in the data.

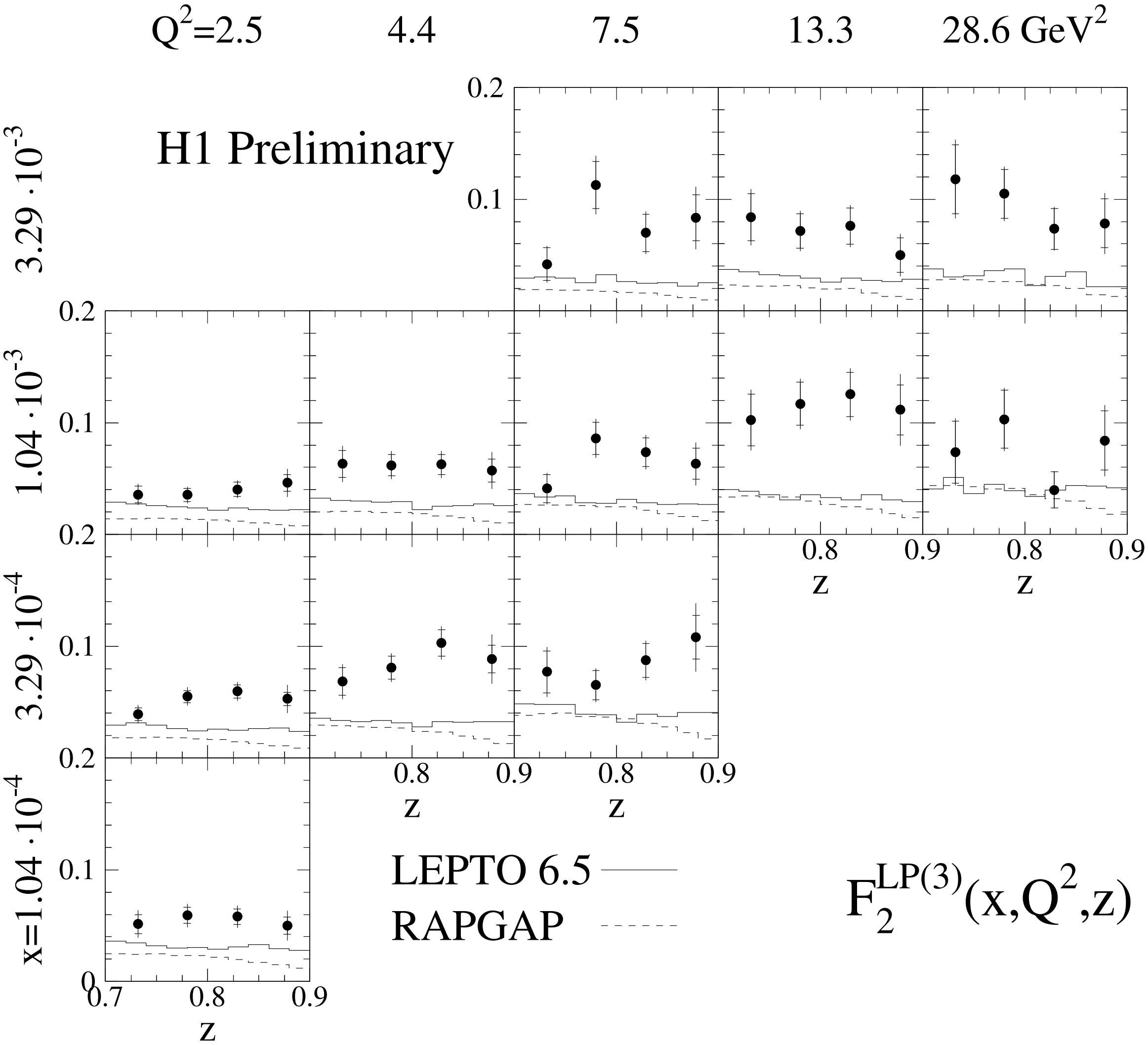

Figure 5: Measurement of $F_2^{LP(3)}$, for protons with $p_T \leq 200$ MeV, compared to the predictions of the LEPTO and RAPGAP Monte Carlo models calculated using GRV leading order parton distributions for the proton and the pion respectively. The inner error bars show the statistical errors and the full error bars show the statistical and systematic errors added in quadrature. There is an additional 5.6% overall normalization uncertainty for the data points which has not been included in the full error bars.

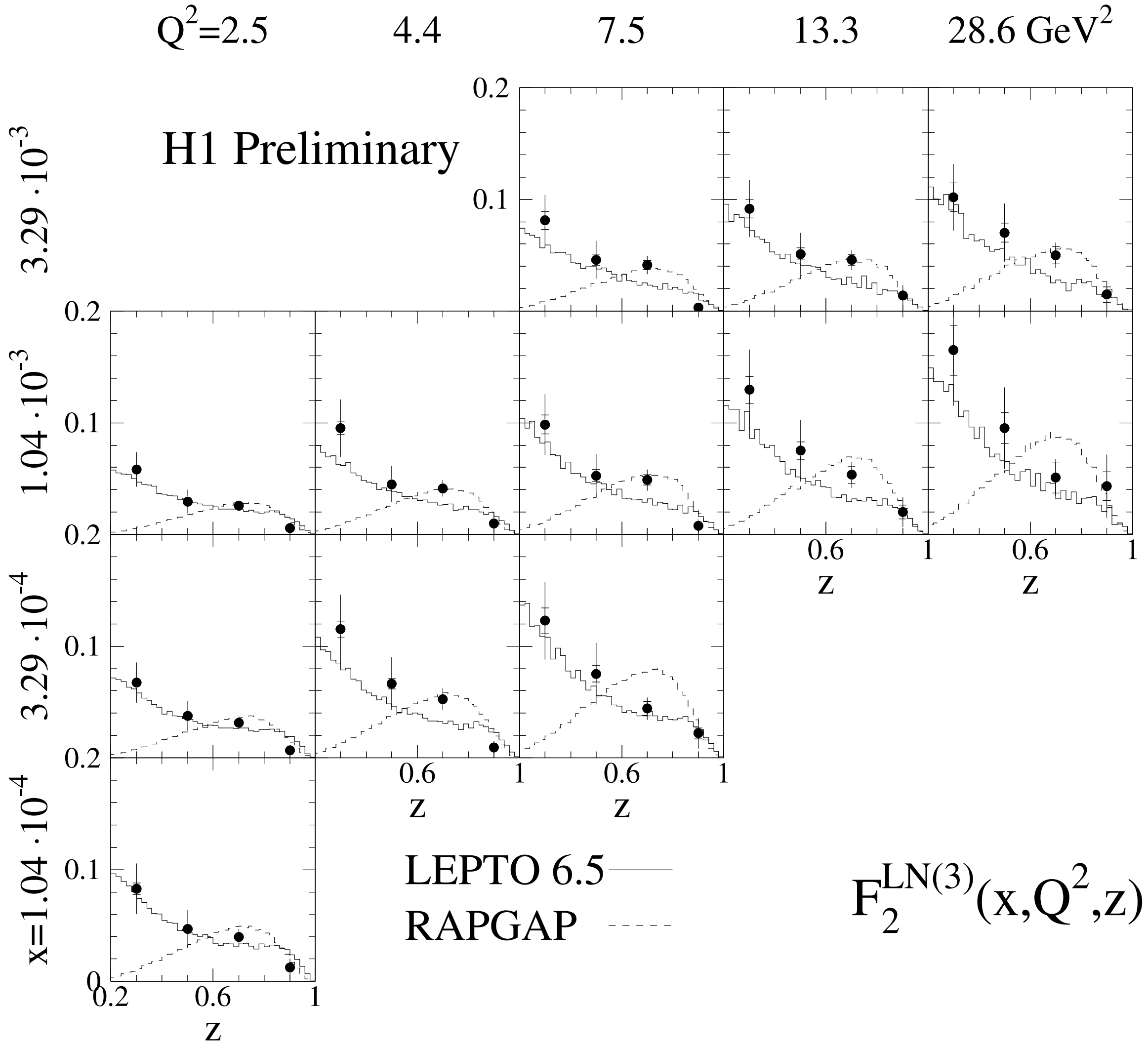

Figure 6: The semi–inclusive structure function $F_2^{LN(3)}$, for neutrons with $p_T \leq 200$ MeV, compared to the predictions of the LEPTO and RAPGAP Monte Carlo models calculated using GRV leading order parton distributions for the proton and the pion respectively. The inner error bars show the statistical errors and the full error bars show the statistical and systematic errors added in quadrature. There is an additional 5.7% overall normalization uncertainty for the data points which has not been included in the full error bars.

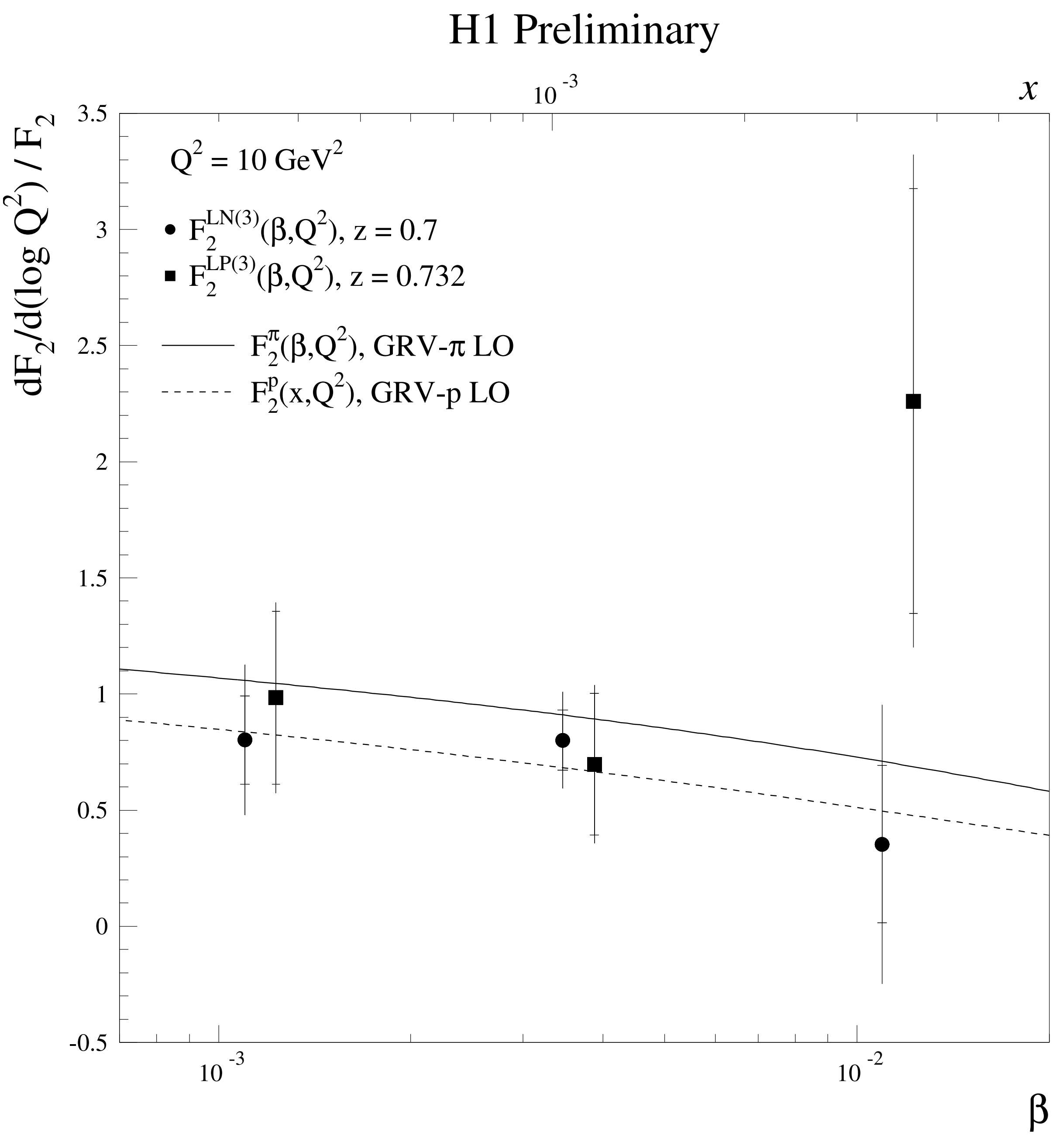

Figure 7: Normalized scaling violations observed in the proton and neutron data, computed at $Q^2 = 10$ GeV^2, compared to the expectations derived from GRV parametrizations of the inclusive structure functions for the pion and the proton. The scaling violations of the pion structure function have been evaluated as a function of β (lower scale), whereas for the proton structure function they have been evaluated as a function of x (upper scale).

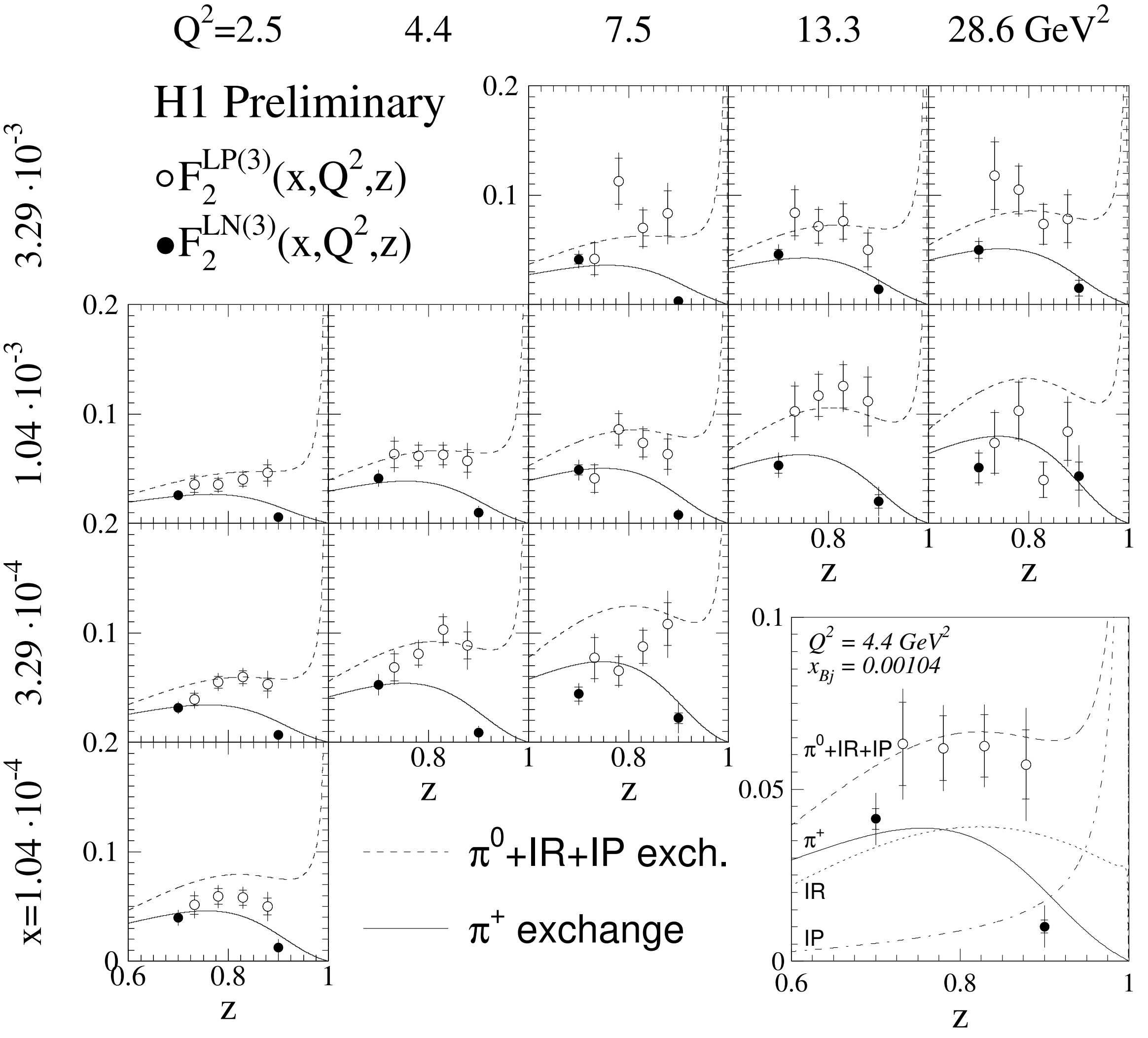

Figure 8: The measured values of $F_2^{LN(3)}$ and $F_2^{LP(3)}$ with $z \geq 0.7$ compared to the Regge model of baryon production. The different contributions are labeled for the figure in the inset. The neutron data are well described by π^+ exchange whereas the proton data are described by the sum of the π^0, pomeron and f_2 exchanges. The π^0 contribution, which is not shown, is exactly half the π^+ contribution.

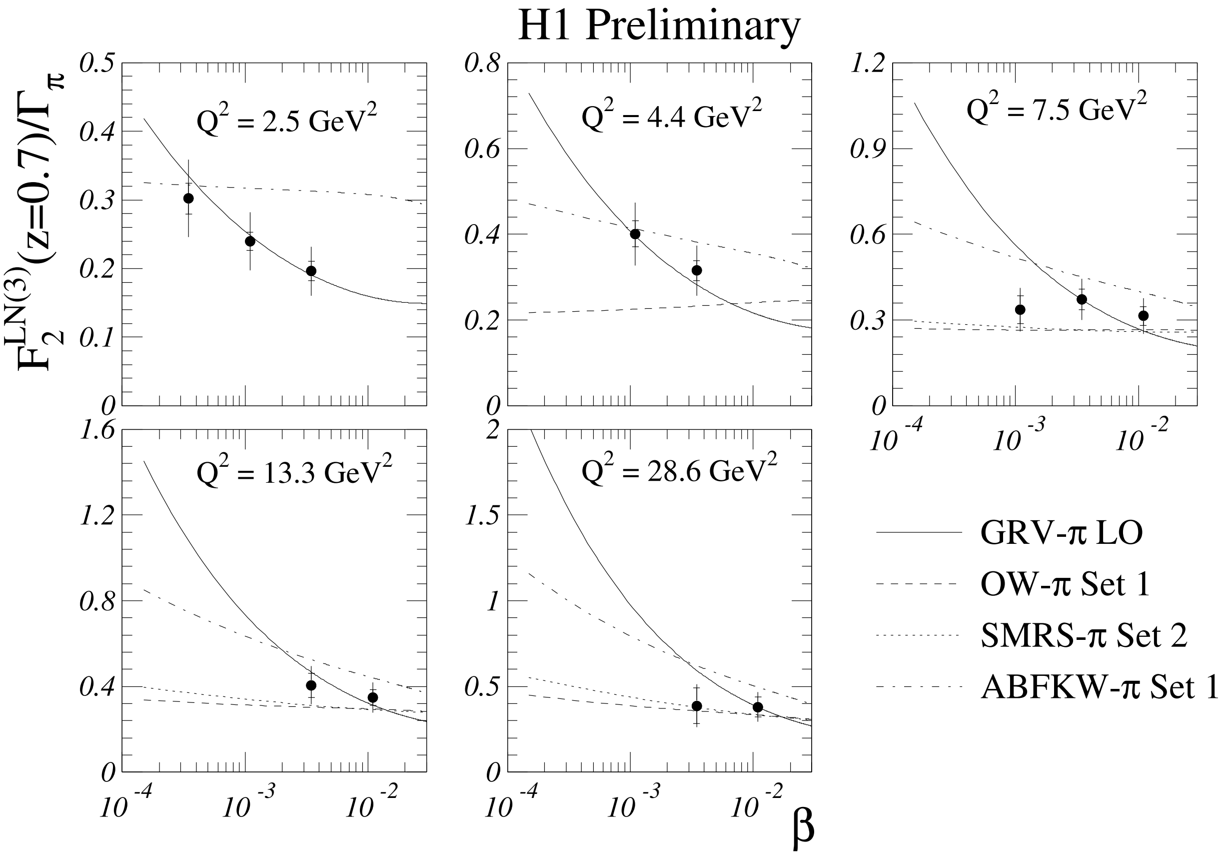

Figure 9: $F_2^{LN(3)}/\Gamma_\pi$ at $z = 0.7$ plotted as a function of β for fixed values of Q^2. The quantity Γ_π is the p_T integrated pion flux factor. Within the framework of the Regge model, $F_2^{LN(3)}/\Gamma_\pi$ can be interpreted as being equal to the pion structure function F_2^π. The data are compared to different parametrizations of F_2^π which are only shown in the Q^2 regions in which they are valid.